

to be submitted to ApJ

Star Formation at Very Low Metallicity. V. The greater importance of initial conditions compared to metallicity thresholds.

Anne-Katharina Jappsen¹

School of Physics and Astronomy, Cardiff University, Cardiff, UK

jappsena@cardiff.ac.uk

Mordecai-Mark Mac Low²

American Museum of Natural History, New York, NY, USA

mordecai@amnh.org

Simon C. O. Glover

*Institut für Theoretische Astrophysik, Zentrum für Astronomie der Universität Heidelberg,
Heidelberg, Germany*

sglover@ita.uni-heidelberg.de

Ralf S. Klessen

*Institut für Theoretische Astrophysik, Zentrum für Astronomie der Universität Heidelberg,
Heidelberg, Germany*

rklessen@ita.uni-heidelberg.de

and

Spyridon Kitsionas³

Astrophysikalisches Institut Potsdam, Potsdam, Germany

skitsionas@gmail.com

¹Fomerly located at the Canadian Institute for Theoretical Astrophysics, Toronto, ON, Canada

²Also at the Max-Planck-Institut für Astronomie and the Institut für Theoretische Astrophysik, Zentrum für Astronomie der Universität Heidelberg, Heidelberg, Germany

³Currently located at Hellenic-American Educational Foundation, Psychiko College, P. Psychiko, Greece

ABSTRACT

The formation of the first stars out of metal-free gas appears to result in stars at least an order of magnitude more massive than in the present-day case. We here consider what controls the transition from a primordial to a modern initial mass function. It has been proposed that this occurs when effective metal line cooling occurs at a metallicity threshold of $Z/Z_{\odot} > 10^{-3.5}$. We study the influence of low levels of metal enrichment on the cooling and collapse of initially ionized gas in small protogalactic halos using three-dimensional, smoothed particle hydrodynamics simulations with particle splitting. Our initial conditions represent protogalaxies forming within a previously ionized H II region that has not yet had time to cool and recombine. These differ considerably from those used in simulations predicting a metallicity threshold, where the gas was initially cold and only partially ionized. In the centrally condensed potential that we study here, a wide variety of initial conditions for the gas yield a monolithic central collapse. Our models show no fragmentation during collapse to number densities as high as 10^5 cm^{-3} , for metallicities reaching as high as $10^{-1} Z_{\odot}$ in one rotating case, far above the threshold suggested by previous work. Rotation allows for the formation of gravitationally stable gas disks over large fractions of the local Hubble time. Turbulence slows the growth of the central density slightly, but both spherically symmetric and turbulent initial conditions collapse and form a single sink particle. We therefore argue that fragmentation at moderate density depends on the initial conditions for star formation more than on the metal abundances present. The actual initial conditions to be considered still need to be determined in detail by observation and modeling of galaxy formation. Metal abundance may still drive fragmentation at very high densities due to dust cooling, perhaps giving an alternative metallicity threshold.

Subject headings: stars: formation – stars: mass function – early universe – hydrodynamics – equation of state – methods: numerical

1. Introduction

Observations of old stellar populations reveal no primordial, metal-free stars (Beers & Christlieb 2005; Frebel, Johnson & Bromm 2007), although the lowest-metallicity stars have abundance distributions suggesting that they may have formed from gas polluted by the ejecta of a single supernova (see e.g. Tominaga, Umeda & Nomoto 2007). Models of primordial star

formation appear to have converged on the result that primordial stars formed with an initial mass function (IMF) very different from modern stars (Abel, Bryan, & Norman 2002; Bromm et al. 2002; O’Shea & Norman 2006; Yoshida *et al.* 2006). Rather than predominantly forming stars with masses similar to or less than the Sun’s, primordial stars seem to have been massive, short-lived, objects.

This raises the question of what controls the transition from the primordial IMF to the modern one. Bromm et al. (2001) performed simulations of the collapse of cold gas in a top-hat potential that included the metallicity-dependent effects of atomic fine structure cooling. In the absence of molecular cooling, they found that fragmentation suggestive of a modern IMF only set in at metallicities above a threshold value of $Z_{\text{th}} \simeq 10^{-4}Z_{\odot}$. However, they noted that the neglect of molecular cooling could be significant. Omukai et al. (2005) argued, based on the results of their detailed one-zone models, that molecular cooling would indeed dominate the cooling over many orders of magnitude in density. Jappsen et al. (2007b, hereafter Paper IV) presented the results of three-dimensional collapse simulations that included molecular cooling modeled using the simplified chemical network described in Glover & Jappsen (2007, hereafter Paper I) and Glover (2008, hereafter Paper III). They found that fragmentation similar to that seen by Bromm et al. (2001) occurs in models starting from the same initial conditions, but with metallicities below the threshold, and indeed even with zero metallicity.

These results suggest that the initial conditions adopted by Bromm et al. (2001) may have determined the result much more than it might have been appreciated at the time. These initial conditions can now be seen to represent not necessarily the predominant mode of early low-metallicity star formation: the gas begins at a redshift of $z = 100$ with its metallicity already set, but with its temperature the same as that of unenriched gas at that redshift, and far below the virial temperature of the halo into which it is eventually incorporated. Furthermore, the dark matter halo itself has no central condensation, but merely local perturbations on a flat, top-hat, potential.

It is therefore important to consider whether a metallicity threshold appears in simulations with different initial conditions than those adopted by Bromm et al. (2001) and Paper IV. In this paper, we examine a different, still idealized, set of initial conditions, and find no fragmentation even at metallicities *above* the claimed threshold. We therefore argue that fragmentation at moderate density depends on the initial conditions for star formation more than on the metal abundances present. The actual initial conditions to be considered still need to be determined in detail by observation and modeling of galaxy formation. Metal abundance may still drive fragmentation at very high densities as suggested by Omukai et al. (2005) and Clark et al. (2008), perhaps giving an alternative metallicity threshold.

In §2 we describe the numerical methods and initial conditions used for our models, while in §3 we describe our results. In §4 we compare our results to earlier work to demonstrate the importance of the environment and initial conditions to the problem.

2. Numerical Methods

2.1. Algorithms

To assess the relative influence of initial conditions and metallicity on the cooling and collapse of gas in small protogalactic halos, we used numerical simulations. During collapse, gas increases in density by several orders of magnitude, and so it is best simulated by a numerical method with a high dynamical range. We therefore chose smoothed particle hydrodynamics (SPH). Overviews of the method, its numerical implementation, and some of its applications are given in reviews by Benz (1990) and Monaghan (1992). We use the parallel SPH code GADGET version 1.1 (Springel et al. 2001) for our simulations.

SPH is a Lagrangian method for simulating astrophysical flows, in which the fluid is represented by an ensemble of particles, with flow quantities at a particular point obtained by averaging over an appropriate subset of neighboring SPH particles. The mass resolution of a simulation is approximately

$$M_{\text{res}} = 2N_{\text{neigh}}m_{\text{p}} \quad (1)$$

where N_{neigh} is the number of particles within a given SPH smoothing kernel and m_{p} the mass of a single gas particle. To avoid numerical fragmentation the Jeans mass M_{J} has to be resolved (Bate & Burkert 1997): $M_{\text{res}} < M_{\text{J}}$. In order to achieve a higher mass resolution, we refine the mass of the gas particles in regions approaching the Jeans criterion using the method of Kitsionas & Whitworth (2002). For details on the implementation of the method see Appendix A.

Particle timesteps are constrained by the Courant-Friedrich-Lewy condition that signals cross no more than a fraction of a resolution element per timestep, so they grow increasingly short as the resolution improves during collapse of high density regions. Replacing dense cores with artificial sink particles therefore leads to a considerable increase in computational speed, allowing the dynamical evolution of the lower-density gas to be followed over multiple free-fall times. In the runs presented here we implement sink particles according to the prescription of Bate et al. (1995). Sink particles are introduced in regions where the density rises above $1.25 \times 10^5 \text{ cm}^{-3}$, and accrete gas within a radius of 0.1 pc. On every timestep, any gas within this accretion radius that is gravitationally bound to the sink particle is accreted by it. The design and implementation of our sink particle algorithm is discussed in more

detail in Jappsen et al. (2005).

2.2. Chemistry and Cooling

2.2.1. Chemical Model

The chemical model used in our simulations is the same as that used in paper IV, and is discussed in more detail in papers I & III. It is designed to accurately follow the major atomic and molecular coolants of the gas. Provided that carbon and oxygen are amongst the most abundant metals, the major coolants will be largely the same as in local atomic and molecular gas, namely H_2 , HD, C, C^+ , O, Si, Si^+ , CO, OH and H_2O (Omukai et al. 2005). We therefore follow the abundances of these ten species, together with an additional 29 species that play important roles in determining the abundances of one or more of these coolants. A full list of the chemical species included is given in Table 1. The chemical network presented in papers I and III contains 189 collisional gas-phase reactions between these 39 species, as well as grain surface reactions, reactions involving the photoionization or photodissociation of chemical species by ultraviolet radiation, and reactions involving cosmic rays. For simplicity, in the simulations presented in this paper we do not include the effects of dust, UV radiation or cosmic rays, and so use a simplified version of the model that contains only the collisional reactions.

To implement this chemical network within GADGET, we make use of operator splitting. During a given SPH particle time-step, we first compute the new SPH densities in the standard fashion, and then update the chemical abundances by solving a coupled set of rate equations of the form

$$\frac{dn_i}{dt} = C_i - D_i n_i, \quad (2)$$

where n_i is the number density of species i , and C_i and D_i are chemical creation and destruction terms that generally depend on the temperature T and the chemical abundances of the other reactants in the system. In our current implementation, we solve rate equations for the abundances of only 18 of our 39 species. The abundances of a further 14 species that have rapid creation and destruction timescales are determined under the assumption that chemical equilibrium applies, while the abundances of the final seven species are determined through the use of conservation laws for charge and elemental abundance. For each chemical species in our model, the method of solution used is summarized in Table 1. To ensure numerical stability, we solve our set of chemical rate equations implicitly, using the DVODE solver (Brown, Byrne, & Hindmarsh 1989), together with an implicit equation for the specific internal energy of the particle (see §2.2.2 below).

2.2.2. Cooling Function

The thermal evolution of the gas in our simulations is modelled using a cooling function that includes the effects of atomic fine structure cooling from C, C⁺, O, Si and Si⁺, rotational and vibrational cooling from H₂, HD, CO and H₂O, Lyman- α cooling, Compton cooling, and H⁺ recombination cooling, as well as a number of other processes of lesser importance. A full list of the processes included is given in Table 2; further details can be found in papers I and III. To allow for the effects of cosmic microwave background (CMB) heating of the gas, we adopt in our simulations a modified cooling rate of the form

$$\Lambda = \Lambda(T) - \Lambda(T_{\text{CMB}}), \quad (3)$$

where $\Lambda(T)$ is the cooling rate of the gas per unit volume for gas temperature T and $\Lambda(T_{\text{CMB}})$ is the cooling rate when $T = T_{\text{CMB}}$. This modification has a negligible effect when $T \gg T_{\text{CMB}}$, but prevents the gas from cooling beneath the floor set by the CMB temperature, except by adiabatic expansion.

To treat radiative cooling within the GADGET framework, we use the same isochoric approximation as Springel et al. (2001). During a given particle time-step, we first compute \dot{u}_{ad} , the rate of change of the internal energy due to adiabatic gas physics. We then solve an implicit equation for the new internal energy:

$$u^{n+1} = u^n + \dot{u}_{\text{ad}}\Delta t - \frac{\Lambda[\rho^n, u^{n+1}]\Delta t}{\rho^n}, \quad (4)$$

where u^n and u^{n+1} are the internal energy per unit mass at time t^n and t^{n+1} respectively, ρ^n is the gas density at time t^n . This implicit equation is solved simultaneously with the chemical rate equations using the DVODE solver.

We ensure that the internal energy of the SPH particle does not change by a large amount during a single timestep by constraining the timestep:

$$\Delta t \leq \eta_c \times \min\left(\frac{u^n}{\dot{u}_{\text{ad}}}, \frac{\rho^n u^n}{\Lambda}\right), \quad (5)$$

where $\eta_c = 0.01$. This limitation is necessary to ensure that the estimates constructed by GADGET of the internal energy and thermal pressure at intermediate points during the timestep are accurate, and hence that the pressure forces acting on particles with shorter timesteps are also computed accurately.

2.3. Initial Conditions

2.3.1. Initial Temperature and Density Distribution

Our initial conditions are based on those used in Jappsen et al. (2007a, hereafter Paper II), although collapse is followed to much higher density in the current work. We study protogalaxies forming from finite metallicity gas with initial temperature $T_g = 10^4$ K, representing a fossil H II region (Oh & Haiman 2003) polluted by supernovae from the ionizing object. Because of the higher mixing rates expected in gas with higher sound speed, such warm gas will have metals mixed into it far earlier than cold primordial gas in the same region. Fossil H II regions subject to cooling and collapse will be common as the characteristic lifetimes of ionizing sources are significantly shorter than the Hubble time even at high redshifts. The gas rapidly cools by emission of Lyman- α radiation and collapses into any low-mass dark matter halos present.

We model one such halo by using a fixed background potential. The potential is spherically symmetric with a density profile (Navarro et al. 1997)

$$\rho_{\text{dm}}(r) = \frac{\delta_c \rho_{\text{crit}}}{r/r_s(1 + r/r_s)^2}, \quad (6)$$

where r_s is a scale radius, δ_c is a characteristic (dimensionless) density and $\rho_{\text{crit}} = 3H^2/8\pi G$ is the critical density for closure. Note that we use a value for the Hubble constant of $H = 72 \text{ km s}^{-1} \text{ Mpc}^{-1}$ (Spergel et al. 2003). Following Navarro et al. (1997) we calculate the characteristic density and the scale radius from a given redshift and dark halo mass. We truncate the halo at the radius at which the value of ρ_{dm} given by Equation 6 equals the cosmological background density at the beginning of the simulation.

In all of the runs presented here, the halo mass is $7.8 \times 10^5 M_\odot$ and the initial redshift is $z = 25$. We truncate the halo at a radius $r_t = 0.49 \text{ kpc}$. The virial temperature of the resulting halo is 1900 K and the virial radius is 0.1 kpc. In physical units, the scale radius of the halo is 29 pc and the full computational volume is a box of side length 1 kpc.

We use periodic boundary conditions for the hydrodynamic part of the force calculations to keep the gas bound within the computational volume. The self-gravity of the gas and the gravitational force exerted by the dark matter potential are not calculated periodically since we assume that other dark matter halos and their gas content are distant enough to neglect their gravitational influence.

We begin our simulations with a uniform distribution of gas with an initial density ρ_g , taken to be equal to the cosmological background density, and then allow the gas to relax isothermally until it reaches hydrostatic equilibrium. This initial phase of the simulation

is merely a convenient way to generate the appropriate initial conditions for the simulation proper, and so we do not include the effects of chemical evolution or cooling during this phase.

The mass of gas present in our simulation was taken to be a fraction $\Omega_b/\Omega_{\text{dm}}$ of the total mass of dark matter, where the dark matter density $\Omega_{\text{dm}} = \Omega_m - \Omega_b$, and where Ω_b is the baryon density and Ω_m is the matter density. We take values for the cosmological parameters from Spergel et al. (2003) of $\Omega_b = 0.047$ and $\Omega_m = 0.29$, giving us a total gas mass of $M_g = 0.19 M_{\text{dm}}$. M_{dm} is the sum of the halo mass and the mass of the dark matter background in the simulated volume, and has a value $M_{\text{dm}} = 1.84 \times 10^6 M_\odot$. Therefore, $M_g = 3.5 \times 10^5 M_\odot$. Initially, we use 1.4×10^5 SPH particles to represent the gas, and so each particle has a mass $m_p = 2.5 M_\odot$. Due to the refinement, the number of particles rises during the simulation up to 9×10^6 , and the SPH particles that represent the gas in the collapsing region have a mass of $m_p = 0.015 M_\odot$ (see Appendix A). Our SPH smoothing kernel encompasses approximately 50 particles and since we need twice this number in order to properly resolve gravitationally bound objects (Bate & Burkert 1997), our mass resolution is $M_{\text{res}} \simeq 100 m_p = 1.5 M_\odot$.

In the runs presented here we introduce sink particles with an accretion radius of 0.1 pc when the density rises above $1.25 \times 10^5 \text{ cm}^{-3}$. At this density M_J exceeds M_{res} as long as $T > 30 \text{ K}$. As this is much smaller than the CMB temperature at $z = 25$, we always satisfy the Bate & Burkert (1997) resolution criterion by a comfortable margin.

We follow the simulations until collapse occurs and a sink forms or as close as possible to a Hubble time within reasonable computing time. The Hubble time at a redshift of $z = 25$ is $\sim 100 \text{ Myr}$. After more than a Hubble time our assumption of an isolated dark matter halo will no longer be valid, since most halos will have undergone at least one major merger or interaction by this time. The dynamical time within the halo varies between 4 Myr in the center and 450 Myr in the outer regions.

2.3.2. Metallicity

We study both zero metallicity gas and gas that has been enriched to $10^{-3} Z_\odot$. A metallicity of $Z = 10^{-3} Z_\odot$ is an upper limit derived from QSO absorption-line studies of the low column density Lyman- α forest at $z \sim 3$ (Pettini 1999). Estimates of the globally-averaged metallicity produced by the sources responsible for reionization are also typically of the order of $10^{-3} Z_\odot$ (see e.g. Ricotti & Ostriker 2004). We also run a model with a metallicity of $Z = 10^{-1} Z_\odot$ to investigate the influence of an even higher metallicity.

In our simulations of metal-enriched gas, we assume that mixing is efficient and that the metals are spread out uniformly throughout the computational domain. We also assume that the relative abundances of the various metals in the enriched gas are the same as in solar metallicity gas; given the wide scatter in observational determinations and theoretical predictions of abundance ratios in very low metallicity gas, this seems to us to be the most conservative assumption. However, variations in the relative abundances of an order of magnitude or less will not significantly alter our results. We have denoted runs with zero metallicity with “Z0” and runs with metallicity with “Z-3” and “Z-1”.

2.3.3. Rotation

We further investigate the influence of rotation on the collapse and possible fragmentation of the gas. Theoretically, we do expect rotation to become important on scales $r \ll \lambda r_{\text{vir}}$, where r_{vir} is the virial radius of the halo and λ is the dimensionless spin parameter, given by (Peebles 1971)

$$\lambda = \frac{J|E|^{1/2}}{GM^{5/2}}, \quad (7)$$

where J is the total angular momentum of the halo, M is the halo mass and E is the total (kinetic plus potential) energy of the halo. Previous work has shown that for halos with the range of masses and redshifts considered in this paper, λ has a lognormal distribution, with mean $\bar{\lambda} = 0.035$ (Yoshida et al. 2003).

In Paper II we showed that rotation has very little effect on the evolution of the gas at early times but it did appear to affect the evolution once the density exceeds $n = 100 \text{ cm}^{-3}$, significantly slowing the collapse. Here we investigate if the rotation results in the formation of a rotationally supported disk.

We perform three simulations in which the initial gas distribution was given a non-zero angular momentum. Within the virial radius of the halo, the gas was placed into rotation with constant angular velocity. At larger radii, the initial angular velocity decreased linearly with radius, reaching zero at the truncation radius of the halo. These runs, which we designate hereafter using “ROT”, had a spin parameter $\lambda = 0.05$.

2.3.4. Turbulence

Finally, we study the influence of low and intermediate levels of turbulence on the evolution of the gas within the dark matter halo. Turbulence establishes a network of interacting

shocks, where converging flows and shear generate filaments of high density. We investigate if the turbulence can provide high density gas that acts as a seed for fragmentation. For one run we assume a turbulent energy of 5% of the internal energy and denote it with “TURB1”, while for two further runs with turbulence we take a value of 10% and denote it with “TURB2”. We have included turbulence in our version of the code that is driven uniformly with the method described by Mac Low et al. (1998) and Mac Low (1999). We insert energy on scales of the order of the size of our computational domain, i.e. with wave numbers $k = 1..2$.

2.3.5. Choice of Parameters

In the choice of parameters, we first restrict ourselves to the primordial case. This enables us to directly compare our results with those of Paper IV and to study the influence of differences in the initial conditions on the dynamical evolution. Since we suspect that the radial symmetry of our initial conditions in run Z0 may artificially suppress fragmentation, we investigate the effects of adding turbulent energy to the gas: a low level of energy in run Z0-TURB1 and a higher level in run Z0-TURB2.

We next investigate the effects of enriching the gas with a low level of metallicity, $Z = 10^{-3} Z_{\odot}$. In this case, we start our investigation with a run which incorporates turbulence at the TURB2 level; since we find no fragmentation in this case, we can reasonably assume that we will not find it in runs with less turbulence, or with the spherical symmetry unbroken. We therefore do not include the corresponding runs Z-3-TURB1, and Z-3 in our analysis.

Finally, we study the effects of rotation. Here we consider three different metallicities, the purely primordial case (Z0-ROT), as well as $Z = 10^{-3} Z_{\odot}$ (Z-3=ROT) and $Z = 10^{-1} Z_{\odot}$ (Z-1-ROT). We add one run with a high metallicity to investigate the influence of the metals in the rotating case more thoroughly. We do not mix turbulence and rotation in any of the models to prevent confusion of the respective effects. A complete list of runs is given in Table 3.

3. Results

In agreement with the results presented in Paper IV, the inclusion of molecular hydrogen cooling largely erases the difference in temperature structure between zero and low-metallicity gas (see Figure 1). Only gas with metallicity as high as $0.1 Z_{\odot}$ cools at substantially lower density than zero metallicity gas, as seen in the rotating models shown in

Figure 2. In all cases, the gas is able to cool down to the CMB temperature at our initial redshift $z = 25$.

In Paper II we found that the centrally concentrated halo profile that we have chosen to study suppressed fragmentation at number densities below 500 cm^{-3} even for metallicities far above the threshold Z_{th} suggested by Bromm et al. (2001). Our current models show no fragmentation during collapse to number densities as high as 10^5 cm^{-3} for metallicities reaching as high as $10^{-1} Z_{\odot}$ in one rotating case.

We consider several different variations on the initial conditions of the gas in order to understand the lack of fragmentation that we find. Model Z0 is a zero metallicity model that collapses spherically, with temperatures dropping to the CMB temperature (see Fig. 1). In Paper IV, we showed that fragmentation proceeds readily at these temperatures and densities in a top-hat potential with small perturbations, even at zero metallicity, but in the centrally concentrated potential studied here, no fragmentation occurs (top panel of Fig. 3). One central sink particle forms and accretes.

3.1. Turbulence

We then consider whether breaking spherical symmetry can lead to fragmentation. To do this, we initialize the gas with two different levels of turbulent kinetic energy (Table 3) in runs Z0-TURB1 and Z0-TURB2. Converging flows effectively produce randomly oriented density perturbations, as shown in the middle panels of Figure 3. However, no further gravitational fragmentation occurs. In the less turbulent TURB1 run, a sink particle forms from collapsing gas during the run, while even that does not occur in the more energetic TURB2 runs. Increasing the metallicity to $Z = 10^{-3} Z_{\odot}$ in run Z-3-TURB2 neither markedly increases the cooling compared to the zero metallicity case (Fig. 1), nor produces fragmentation (bottom panel of Fig. 3).

3.2. Rotation

Up to this point organized rotation has not been introduced into our models. Disk formation naturally leads to fragmentation and the formation of multiple stellar systems in present-day star formation (e.g. Matsumoto et al. 1997), so we investigate whether it could play a similar role in this situation. In Figure 4 we show horizontal and vertical number density cross sections of runs in this parameter study. We find that thin disk formation proceeds only in the Z-1-ROT case, with metallicity $Z = 0.1 Z_{\odot}$. In models Z0-ROT and

Z-3-ROT, with metallicity on either side of the threshold Z_{th} , however, the gas cannot cool strongly enough to form a thin disk, and merely forms a slightly flattened, pressure-supported structure. In none of these three models does fragmentation set in, nor does the central density even grow fast enough for a sink particle to form within 60 Myr, a significant fraction of a Hubble time at that redshift.

4. Discussion

The basic thermodynamic behavior shown in Figures 1 and 2 underlies our conclusion both in Paper IV and here that the introduction of metal line cooling does not yield a substantial difference in star formation behavior once H_2 and HD cooling is also taken into account. Recall that the fragmentation threshold found by Bromm et al. (2001) occurred in simulations neglecting these coolants.

In the centrally condensed potential that we study here, a wide variety of initial conditions for the gas yield a monolithic central collapse. Figures 5 and 6 show that the central density depends on the initial conditions. Turbulence slows the growth of the central density slightly (Fig. 5), but both spherically symmetric and turbulent initial conditions collapse and form a sink particle. The mass in dense gas (over an arbitrary value of $n_{\text{thres}} = 10^3 \text{ cm}^{-3}$) grows rapidly in both cases once collapse sets in (Fig. 5).

Rotation allows for the formation of stable disks over large fractions of the local Hubble time. Figure 6 shows that once a rotationally supported structure has formed, the central density and amount of mass at high density ceases to grow quickly. This is because the continued growth of the central density now depends on angular momentum transport within the rotating structure. Molecular viscosity is sufficiently low that no further accretion would happen at all if that were the only cause of transport. In modern star formation, the additional transport in circumstellar disks occurs because of magnetorotational instability (Balbus & Hawley 1998) or gravitational instability (Gammie 2001). However, our models include no magnetic fields, so the magnetorotational instability cannot act here.

4.1. Gravitational Instability

To examine whether gravitational instability may be important in driving accretion or fragmentation, we examine the value of the Toomre (1964) instability parameter

$$Q = \kappa c_s / \pi G \Sigma, \quad (8)$$

where G is Newton’s gravitation constant, Σ is the disk surface density, κ is the epicyclic frequency, and c_s is the sound speed. Radial gravitational instability occurs for $Q < 1$. In Figure 7 we examine our rotating runs. We see that, in agreement with the observed lack of fragmentation, the disks are strongly Toomre stable for the first 50 Myr, with $Q > 10$ throughout, and only begin to reach the unstable regime at the very center thereafter.

In fact, given the lack of gravitational instability or magnetic fields, the accretion towards the center seen in the simulation still represents only an upper limit on the actual accretion rate, as all the angular momentum transfer occurring must be due to numerical viscosity. In reality, virtually all galaxies interact with other galaxies over the course of a Hubble time. The resulting tidal perturbations drive strong accretion and subsequent star formation. Our results suggest that, at least at early times when only small halos are collapsing, galaxy interactions may be essential for driving star formation.

Another way of looking at the development of gravitational instability is to examine the total number of Jeans masses at every number density, as it is shown in Figure 8. This compares the standard primordial run Z0 to the highest metallicity rotating run Z-1-ROT. Whereas Z0 reaches Jeans number unity at the highest densities at $t > 55$ Myr, Z-1-ROT only approaches Jeans number unity at lower densities $n \sim 100 \text{ cm}^{-3}$. This gas is widely distributed away from the center of the disk, however, so it cannot collect and collapse towards a common center. Too little material reaches the high densities at the very center of the disk to start runaway collapse there.

4.2. Metallicity Thresholds

How does our result agree with other work on low-metallicity star formation? We have already discussed the comparison with Bromm et al. (2001). The same authors examined their zero metallicity case in the absence of an ambient UV radiation sufficient to dissociate H_2 , so that molecules can form and contribute to the cooling. They found the same result as was later reached by Paper IV, that the top hat potential does lead to fragmentation even at zero metallicity (Bromm et al. 2002).

A more advanced computation was performed by Smith & Sigurdsson (2007), who used the adaptive mesh grid code Enzo (O’Shea et al. 2004) and a comprehensive treatment of metal cooling rates as detailed by Smith et al. (2008a). Instead of a top-hat dark matter potential, they used cosmological initial conditions, with collapse followed over 28 levels of refinement. Like Bromm et al. (2002) they assumed no dissociating radiation and full molecular cooling. As a result of their choice of initial conditions, their collapsing objects

were centrally concentrated, similar to ours. In agreement with our results, they found no fragmentation below densities of 10^5 cm^{-3} . At higher densities of 10^8 cm^{-3} , they did see hints of fragmentation of their central object into two to four objects at metallicities $Z > 10^{-4} Z_{\odot}$, but that alone seems insufficient to mark a shift from a primordial to a modern initial mass function.

Following up on that work Smith et al. (2008b) presented a suite of simulations investigating the critical metallicity threshold. Two of their runs show fragmentation below densities of 10^5 cm^{-3} into 2 bound clumps but most of their runs show fragmentation at higher densities. Their set of models which collapses at a redshift similar to the one used in our calculations only results in 2 fragments at a metallicity of $Z = 10^{-3.5} Z_{\odot}$ and $Z = 10^{-2} Z_{\odot}$. These differences could also be due to the different initial conditions used. Our simulations began with hot, ionized gas, whereas their simulations started with cold neutral gas. In Paper II we explained the consequences of these differences in more detail. In agreement with Smith et al. (2008b) we also find that the gas reaching the CMB temperature results in a thermally stable gas cloud.

Schneider et al. (2002, 2006) and Omukai et al. (2005) propose that rather than atomic or molecular line cooling determining the metallicity where strong fragmentation sets in, dust continuum cooling does so. Surprisingly, their estimates of cooling rates suggest that fragmentation at high densities $n > 10^{10} \text{ cm}^{-3}$ already sets in for metallicities as low as $Z > 10^{-6} Z_{\odot}$. Omukai et al. (2005) demonstrates that even at these low metallicities, dust cooling gives an effective adiabatic index under unity for a range of densities $10^{10} < n < 10^{14} \text{ cm}^{-3}$, promoting rapid fragmentation of objects collapsing through that density range.

High resolution nested-grid models by Machida et al. (2008) show binaries forming even at primordial metallicity $Z = 0$ at densities $n > 10^{16} \text{ cm}^{-3}$. Machida (2008) then found that binary fragmentation is actually enhanced at decreasing metallicity, with the rotation threshold for fragmentation at $Z = 0$ lying a full two orders of magnitude lower than for solar metallicity $Z = Z_{\odot}$. Low metallicity fragmentation occurs at densities as high as 10^{16} cm^{-3} for $Z = 0$, in contrast to modern star formation where binaries only form for $10^{11} < n < 10^{15} \text{ cm}^{-3}$. However, primordial binary formation still yields very massive stars, simply in pairs rather than alone.

Further simulation of collapsing cores using the Omukai et al. (2005) equation of state has shown that fragmentation promoted by dust cooling at high densities indeed appears able to shift star formation from a primordial to a more present-day-like initial mass function. Tsuribe & Omukai (2006) followed fragmentation of low metallicity $Z < 10^{-4} Z_{\odot}$, high density $n > 10^{10} \text{ cm}^{-3}$ gas in the non-rotating case. Clark et al. (2008) included rotation, and used sink particles to follow the collapse of a complete cluster. They agree with

Machida et al. (2008) in finding only small numbers of high-mass fragments in the primordial case, but already at metallicities of $Z \sim 10^{-5} Z_{\odot}$, they find an average mass under $1 M_{\odot}$, approaching a modern initial mass function.

Dust cooling looks likely to be the primary physics determining the shift in typical stellar mass from primordial to modern stars, with a threshold of $Z \sim 10^{-5} Z_{\odot}$ consistent with the lowest metallicity stars observed in the modern galaxy. Conversely, as we have shown in Paper IV and this paper, atomic line cooling does not appear to dominate this transition, and it appears unlikely that the transition occurs at metallicities as high as $Z = 10^{-3} Z_{\odot}$.

This research was supported in part by the National Science Foundation under Grant No. PHY05-51164. AKJ acknowledges support by the Human Resources and Mobility Programme of the European Community under the contract MEIF-CT-2006-039569. M-MML was partly supported by stipends from the Max-Planck-Gesellschaft and the Deutsche Akademische Austausch Dienst, and acknowledges the hospitality of the Waldkindergarten Heidelberg during the initial drafting of this paper. RSK acknowledges support from the German science foundation under the Emmy Noether grant KL1358/1 and the Priority Program SFB 439 *Galaxies in the Early Universe*. SCOG acknowledges funding from the Germany science foundation via grant KL1358/4. SK kindly acknowledges support by an EU Commission "Marie Curie Intra-European (Individual) Fellowship" of the 6th Framework Programme with contract number MEIF-CT-2004-011226. Computations were performed at the McKenzie cluster at the Canadian Institute for Theoretical Astrophysics and the Sanssouci cluster at the Astrophysikalisches Institut Potsdam. Figures 3 and 4 were produced using SPLASH, a visualization package for SPH written by Price (2007).

A. Particle splitting

In Paper II we presented low-resolution simulations that showed that the density increases most rapidly close to the center of the dark matter halo. On-the-fly splitting (Kitsionas & Whitworth 2002) with two levels of refinement at 2 different radii provides us with the highest mass resolution at the region of interest. Every SPH particle that crosses a radius r_1 of 0.3 kpc towards smaller radii acts as a parent particle and spawns 13 child particles with a mass of $m_p/13$. The same happens at a radius r_2 of 0.2 kpc where gas particles crossing r_2 are split again. The mass of the gas particles within r_2 is thus $m_p/169 \approx 1.5 \times 10^{-2} M_{\odot}$. In the region of collapse we can thus resolve Jeans masses down to $1.5 M_{\odot}$, as compared to $M_{\text{res}} = 200 M_{\odot}$ in the low resolution simulations. Each child particle inherits directly velocity, internal energy and fractional abundances of the chemical

species. Subsequently the child particles are evolved with standard SPH procedures. The only difference is that, to mitigate interactions between adjacent particles having different masses, we have modified the scheme by which GADGET calculates the smoothing lengths of particles. We now evolve h_i , the smoothing length for particle i , so that the radius h_i contains between $N_{\text{neigh}} - N_{\text{dev}}$ and $N_{\text{neigh}} + N_{\text{dev}}$, where N_{dev} is the allowed deviation in the number of neighbors, as well as a mass between $N_{\text{neigh}} - N_{\text{dev}}$ and $N_{\text{neigh}} + N_{\text{dev}}$ times the mass of particle i . If both conditions cannot be satisfied simultaneously we allow for a larger number of neighbors or a larger amount of mass within a sphere of radius h_i . For one specific set of parameters we carried out two simulations, one with the refinement technique and the other without it, and verified that temporal perturbations caused by refinement do not affect the results presented in Section 3.

REFERENCES

- Abel, T., Bryan, G. L., & Norman, M. L. 2002, *Science*, 295, 93
- Aldrovandi, S. M. V. & Pequignot, D. 1973, *A&A*, 25, 137
- Balbus, S. A., & Hawley, J. F. 1998, *Rev. Mod. Phys.*, 70, 1
- Bate, M. R., Bonnell, I. A., & Price, N. M. 1995, *MNRAS*, 277, 362
- Bate, M. R. & Burkert, A. 1997, *MNRAS*, 288, 1060
- Beers, T. C., & Christlieb, N. 2005, *ARA&A*, 43, 531
- Benz, W. 1990, in *Numerical Modelling of Nonlinear Stellar Pulsations Problems and Prospects*, ed. J. R. Buchler (Dordrecht: Kluwer), 269
- Bray, I., Burgess, A., Fursa, D. V., & Tully, J. A. 2000, *A&AS*, 146, 481
- Bromm, V., Ferrara, A., Coppi, P. S., & Larson, R. B. 2001, *MNRAS*, 328, 969
- Bromm, V., Coppi, P. S., & Larson, R. B. 2002, *ApJ*, 564, 23
- Brown, P. N., Byrne, G. D., & Hindmarsh, A. C. 1989, *SIAM J. Sci. Stat. Comput.*, 10, 1038
- Cen, R. 1992, *ApJS*, 78, 341
- Clark, P. C., Glover, S. C. O., & Klessen, R. S. 2008, *ApJ*, 672, 757
- Einasto, J. 1965, *Trudy Inst. Astrofiz. Alma-Ata*, 5, 87

- Ferland, G. J., Peterson, B. M., Horne, K., Welsh, W. F., & Nahar, S. N. 1992, *ApJ*, 387, 95
- Frebel, A., Johnson, J. L., & Bromm, V. 2007, *MNRAS*, 380, 40
- Gammie, C. F. 2001, *ApJ*, 553, 174
- Gao, L., Navarro, J. F., Cole, S., Frenk, C., White, S. D. M., Springel, V., Jenkins, A., Neto, A. F. 2008, *MNRAS*, 387, 536
- Glover, S. C. O. 2008, in preparation. (Paper III)
- Glover, S. C. O., & Jappsen, A.-K. 2007, *ApJ*, 666, 1 (Paper I)
- Hummer, D. G., & Storey, P.J. 1998, *MNRAS*, 297, 1073
- Janev, R. K., Langer, W. D., Evans, K., & Post, D. E. 1987, *Elementary Processes in Hydrogen-Helium Plasmas*, Springer
- Jappsen, A.-K., Klessen, R. S., Larson, R. B., Li, Y., & Mac Low, M.-M. 2005, *A&A*, 435, 611
- Jappsen, A.-K., Glover, S. C. O., Klessen, R. S., & Mac Low, M.-M. 2007a, *ApJ*, 660, 1332 (Paper II)
- Jappsen, A.-K., Klessen, R. S., Glover, S. C. O., & Mac Low, M.-M. 2007b, *arXiv:0709.3530* (Paper IV)
- Kitsionas, S. & Whitworth, A. P. 2002, *MNRAS*, 330, 129
- Le Bourlot, J., Pineau des Forêts, G., & Flower, D. R. 1999, *MNRAS*, 305, 802
- Lipovka, A., Núñez-López, R., & Avila-Reese, V. 2005, *MNRAS*, 361, 850
- Mac Low, M.-M., Klessen, R. S., Burkert, A., Smith, M. D. 1998, *Phys. Rev. Lett.*, 80, 2754
- Mac Low, M.-M. 1999, *ApJ*, 524, 169
- Machida, M. N. 2008, *ApJ*, 682, L1
- Machida, M. N., Omukai, K., Matsumoto, T., & Inutsuka, S.-I. 2008, *ApJ*, 677, 813
- Matsumoto, T., Hanawa, T., & Nakamura, F. 1997, *ApJ*, 478, 569
- Merritt, D., Graham, A. W., Moore, B., Diemand, J., Terzić, B., 2006, *AJ*, 132, 2685

- Monaghan, J. J. 1992, *ARA&A*, 30, 543
- Monaghan, J. J. 2005, *Rep. Prog. Phys.*, 68, 1703
- Navarro, J. F., Frenk, C. S., & White, S. D. M. 1997, *ApJ*, 490, 493
- Navarro, J. F., Hayashi, E.; Power, C., Jenkins, A. R., Frenk, C. S., White, S. D. M., Springel, V., Stadel, J. & Quinn, T. R. 2004, *MNRAS*, 349, 1039
- Neufeld, D. A., & Kaufman, M. J. 1993, *ApJ*, 418, 263
- Neufeld, D. A., Lepp., S., & Melnick, G. J. 1995, *ApJS*, 100, 132
- Oh, S. P. & Haiman, Z. 2003, *MNRAS*, 346, 456
- Omukai, K., Tsuribe, T., Schneider, R., & Ferrara, A. 2005, *ApJ*, 626, 627
- O’Shea, B. W., Bryan, G., Bordner, J., Norman, M. L., Abel, T., Harkness, R., & Kritsuk, A. 2004, in *Adaptive Mesh Refinement—Theory and Applications*, eds. T. Plewa, T. Linde, & V. G. Weirs (Berlin, Springer), 341
- O’Shea, B. W., & Norman, M. L. 2006, *ApJ*, 654, 66
- Pavlovski, G., Smith, M. D., Mac Low, M.-M., & Rosen, A. 2002, *MNRAS*, 337, 477
- Peebles, P. J. E. 1971, *A&A*, 11, 377
- Pettini, M. 1999, in *Chemical Evolution from Zero to High Redshift*, eds. J. R. Walsh, M. R. Rosa, (Berlin: Springer), 233
- Prada, F., Klypin, A. A., Simonneau, E., Betancort-Rijo, J., Patiri, S., Gottlber, S., Sanchez-Conde, M. A. 2006, *ApJ*, 645, 1001
- Price, D. J. 2007, *PASA*, 24, 159
- Ricotti, M. & Ostriker, J. P. 2004, *MNRAS*, 350, 539
- Ripamonti, E., & Abel, T. 2004, *MNRAS*, 348, 1019
- Schneider, R., Ferrara, A., Natarajan, P., & Omukai, K. 2002, *ApJ*, 571, 30
- Schneider, R., Omukai, K., Inoue, A. K., & Ferrara, A. 2006, *MNRAS*, 369, 1437
- Shapiro, P. R., & Kang, H. 1987, *ApJ*, 318, 32
- Smith, B. D., & Sigurdsson, S. 2007, *ApJ*, 661, L5

- Smith, B. D., Sigurdsson, S., & Abel, T. 2008, MNRAS, 385, 1443
- Smith, B. D., Turk, M. J., Sigurdsson, S., O’Shea, B. W. & Norman, M. L. 2008, accepted by ApJ, arXiv:0806.1653v2
- Spergel, D. N., Verde, L., Peiris, H. V., et al. 2003, ApJS, 148, 175
- Springel, V., Yoshida, N., & White, S. D. M. 2001, New Astron., 6, 79
- Springel, V. 2005, MNRAS, 364, 1105
- Tominaga, N., Umeda, H., & Nomoto, K. 2007, ApJ, 660, 516
- Toomre, J. 1964, ApJ, 139, 1217
- Tsuribe, T., & Omukai, K. 2006, ApJ, 642, L61
- Yoshida, N., Abel, T., Hernquist, L., & Sugiyama, N. 2003, ApJ, 592, 645
- Yoshida, N., Omukai, K., Hernquist, L., & Abel, T. 2006, ApJ, 652, 6

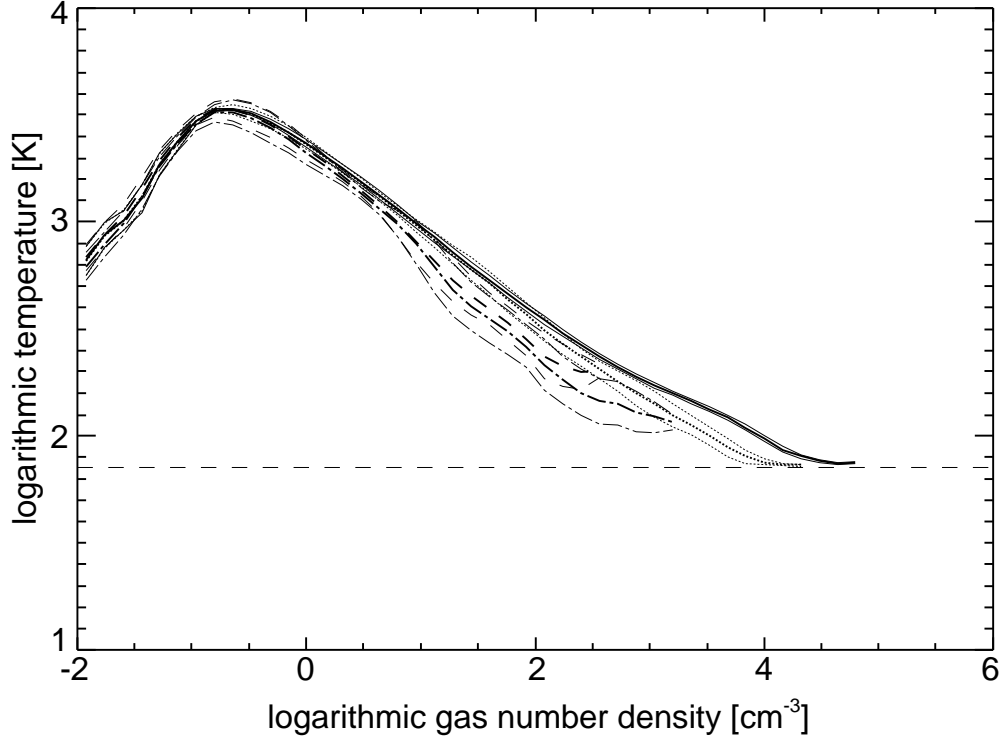


Fig. 1.— Gas temperature vs. number density for runs Z0 (*solid line*), Z0-TURB1 (*dotted line*), Z0-TURB2 (*dashed line*), and Z-3-TURB2 (*dot-dashed line*). The thin lines show the 1σ -deviation around the mean. The time of all plots is $t = 52$ Myr, except for plot Z0-TURB2, which is at $t = 50$ Myr. We show the CMB temperature with the horizontal dashed line. Runs Z0 and Z0-TURB1 reach the CMB temperature in $t = 52$ Myr just from H_2 cooling despite their lack of metals. On the other hand, run Z-3-TURB2, which has a higher fraction of turbulent energy, does not reach the CMB temperature in $t = 52$ Myr despite having metallicity $Z = 10^{-3} Z_{\odot}$.

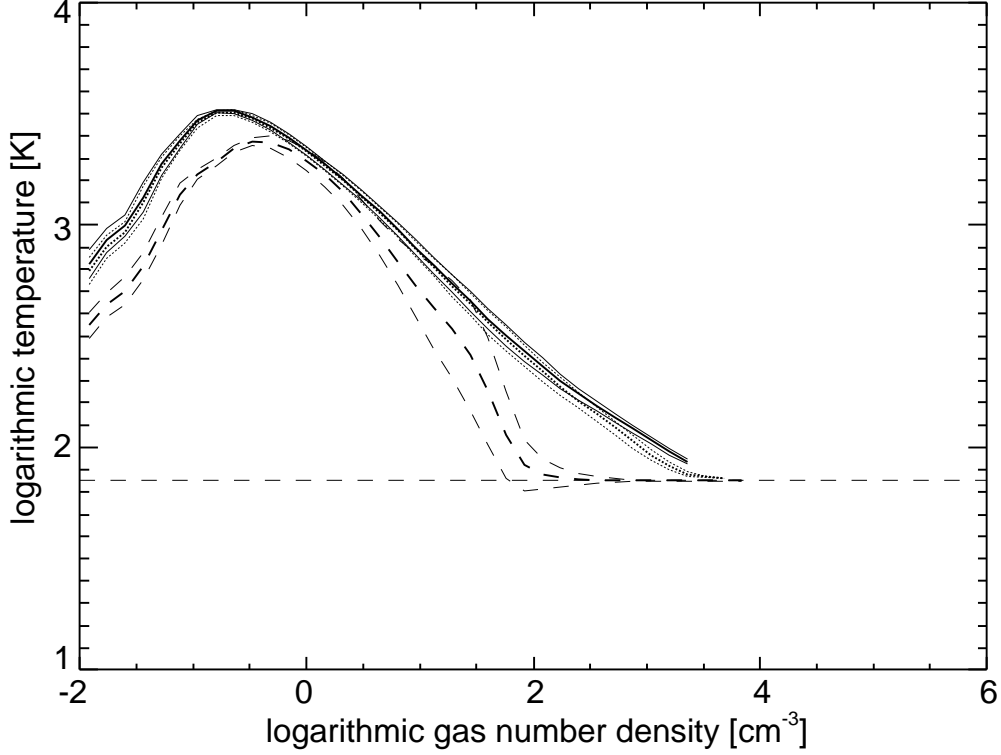


Fig. 2.— Gas temperature vs. number density for runs Z0-ROT (*solid line*), Z-3-ROT (*dotted line*), and Z-1-ROT (*dashed line*). The thin lines show the 1σ -deviation. The halos with rotation have a spin parameter of 0.05. The time of the plots is $t = 52$ Myr. We show the CMB temperature with the horizontal dashed line. The run Z-1-ROT reaches the CMB temperature at a relatively low density value due to the high content of metals that contribute effectively to the cooling. The other two runs show only little difference at higher densities due to the metallicity of run Z-3-ROT.

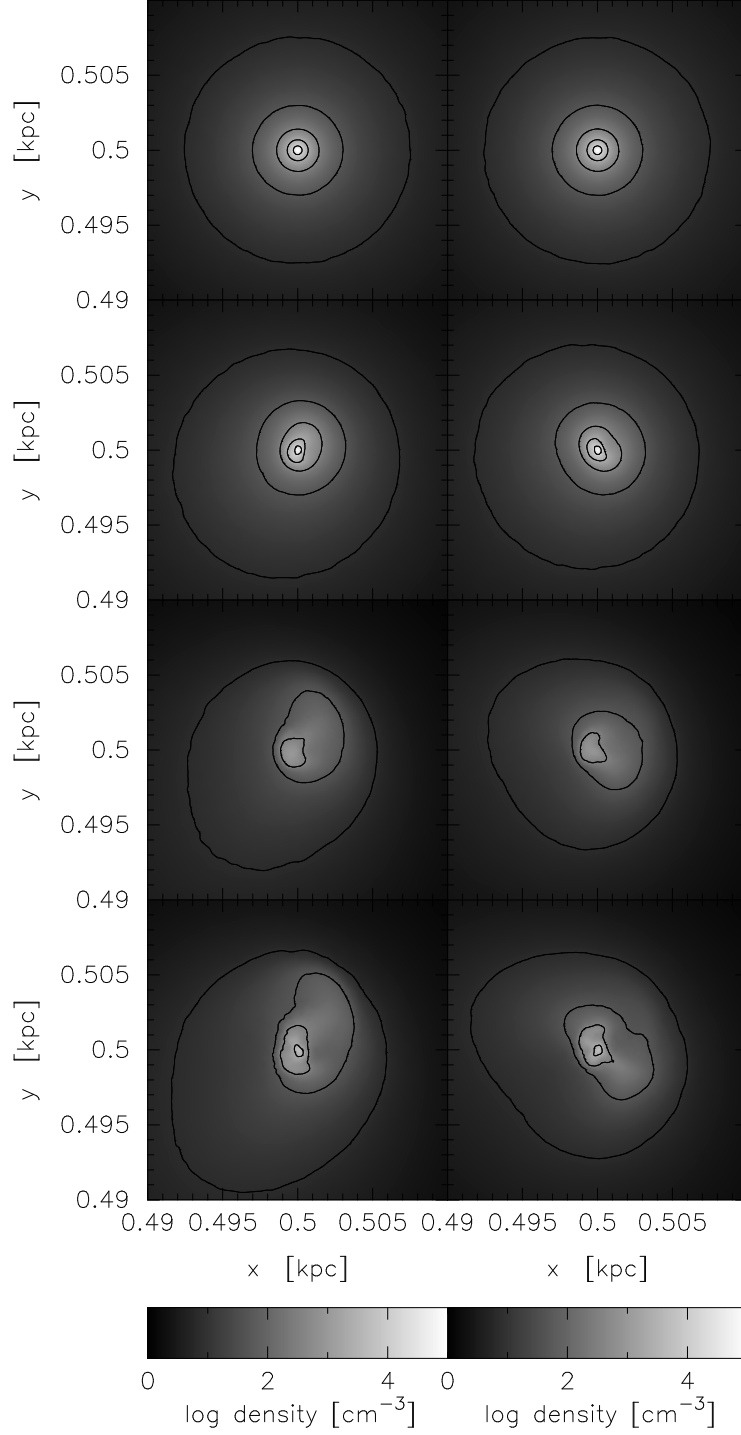


Fig. 3.— *From top to bottom:* Cross sections showing number density for runs Z0, Z0-TURB1, Z0-TURB2, and Z-3-TURB2 at 50 Myr. *Left:* x-y plane, cut at $z = 0.5$ kpc. *Right:* x-z plane, cut at $y = 0.5$ kpc.

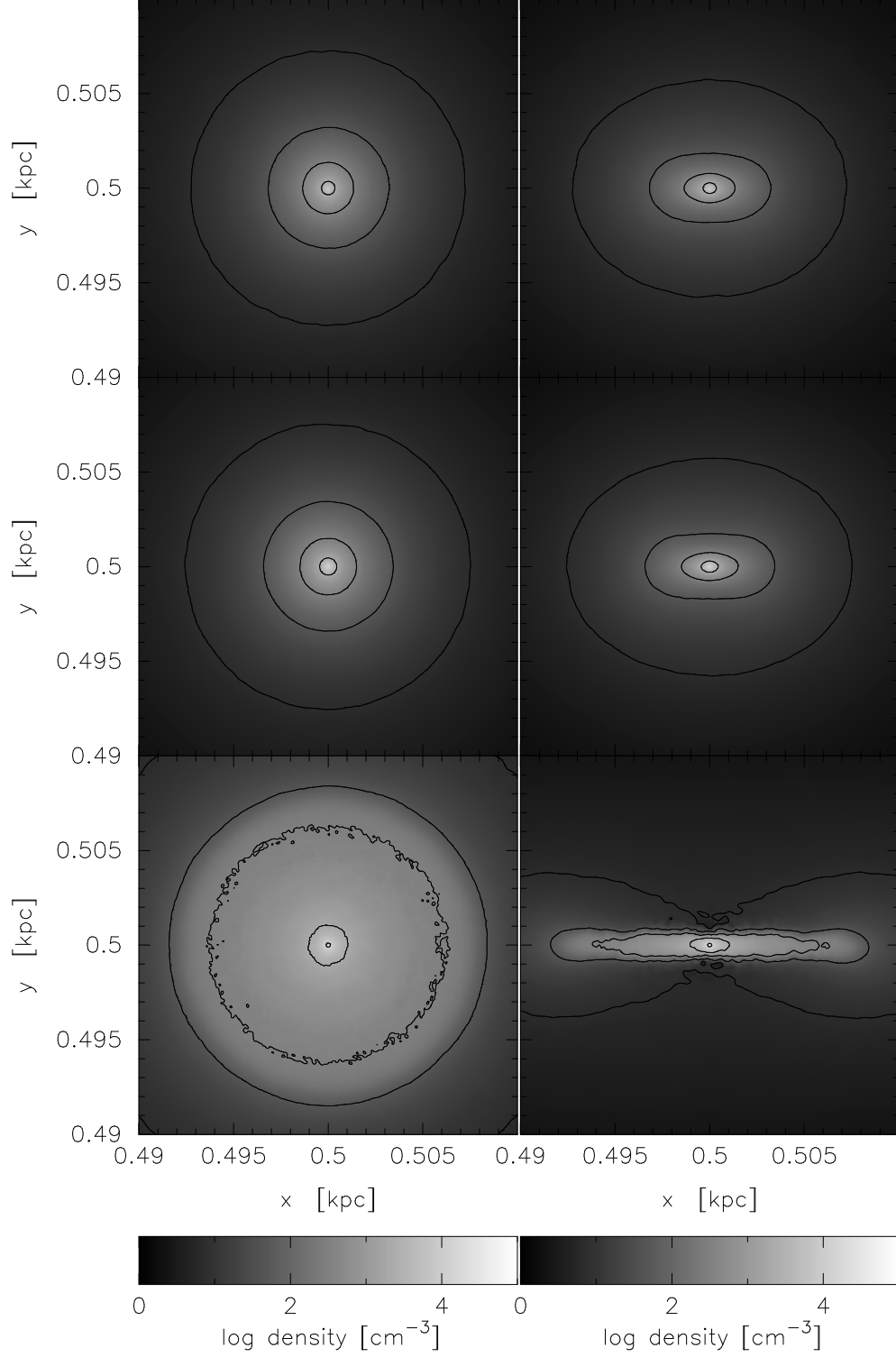


Fig. 4.— *From top to bottom:* Cross sections showing number density for runs Z0-ROT, Z-3-ROT, and Z-1-ROT, at 50 Myr. *Left:* x-y plane, cut at $z = 0.5$ kpc. Face-on view. *Right:* x-z plane, cut at $y = 0.5$ kpc. Edge-on view.

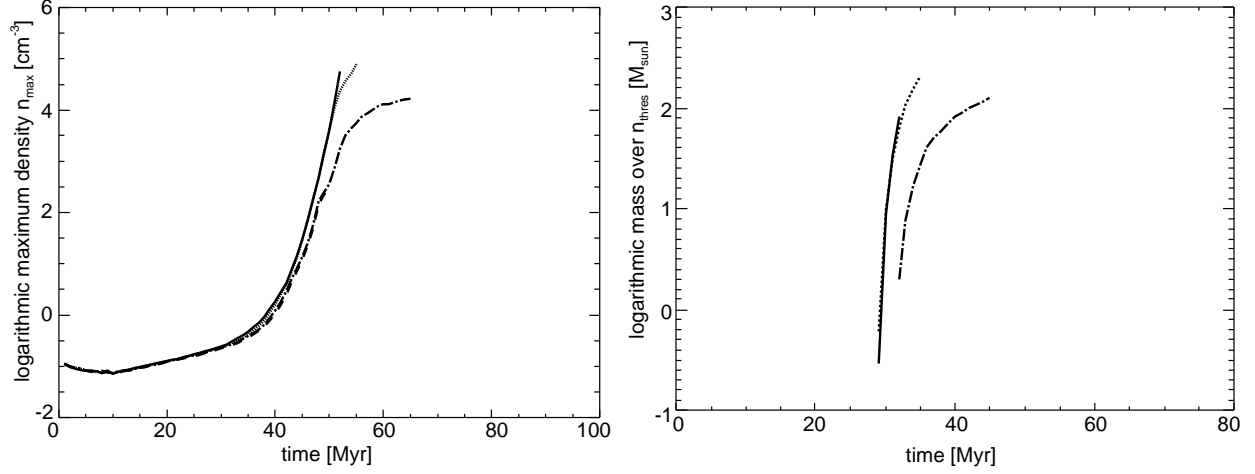


Fig. 5.— *Left panel:* Maximum gas number density vs time for runs Z0 (*solid line*), Z0-TURB1 (*dotted line*), Z0-TURB2 (*dashed line*), and Z-3-TURB2 (*dot-dashed line*). *Right panel:* Mass over density threshold $n_{\text{thres}} = 10^3 \text{ cm}^{-3}$.

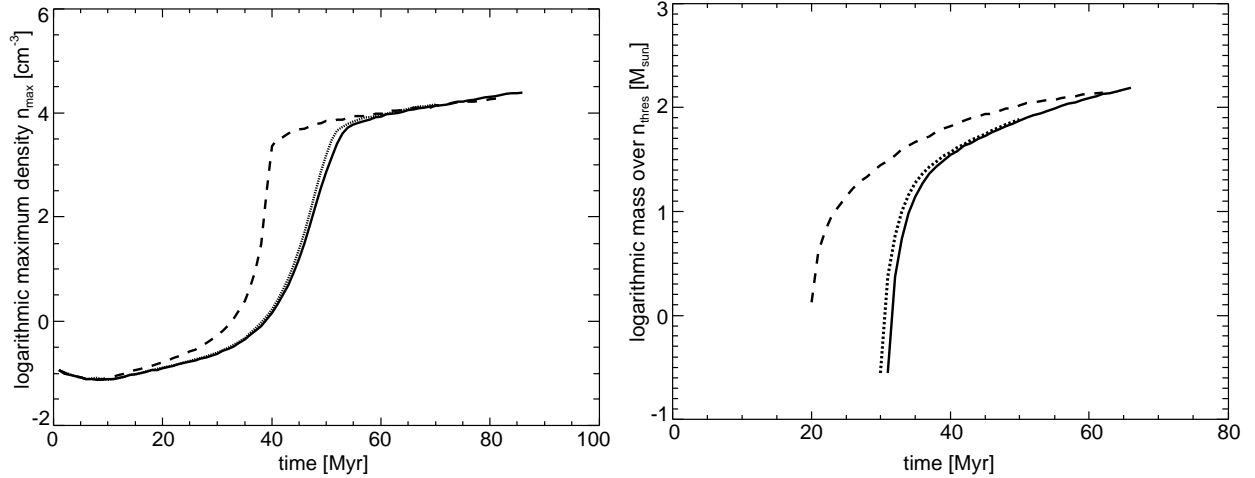


Fig. 6.— *Left panel:* Maximum gas number density vs time for runs Z0-ROT (*solid line*), Z-3-ROT (*dotted line*), and Z-1-ROT (*dashed line*). *Right panel:* Mass over density threshold $n_{\text{thres}} = 10^3 \text{ cm}^{-3}$.

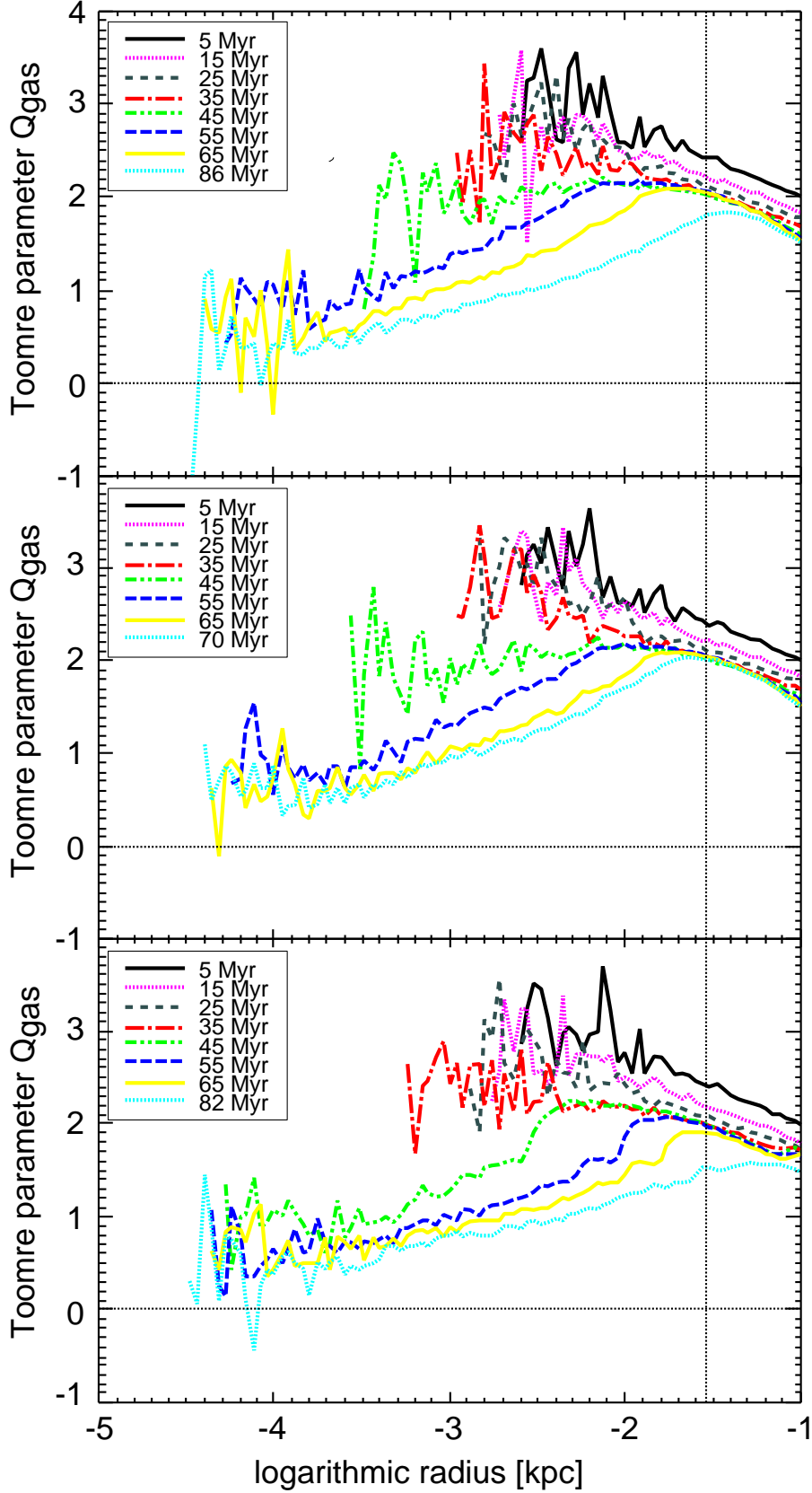


Fig. 7.— *From top to bottom:* Radial distribution of the Toomre parameter Q for the runs with rotation Z0-ROT, Z-3-ROT, and Z-1-ROT. The value of Q is shown on a \log_{10} scale.

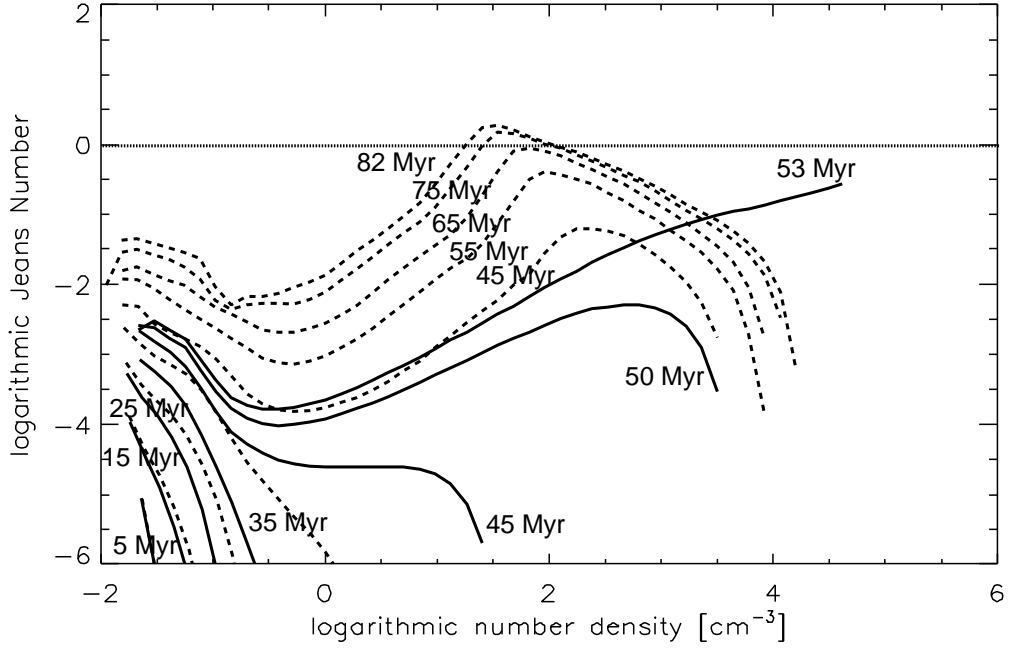


Fig. 8.— We show the temporal evolution of the number of Jeans masses as a function of number density for the runs Z0 (*solid lines*) and Z-1-ROT (*dashed lines*). The runs Z-1-ROT reach a Jeans number of 1 (*dot-dashed horizontal line*) but not at the high number densities that are required for efficient cooling and collapse. In contrast the runs Z0 show a clear trend of the Jeans number rising with time at high densities. The data are equally spaced in logarithmic number density with a bin size of 0.14.

Table 1.

Species	Method of solution
e^-	Conservation law
H^+	Rate equation
H	Conservation law
H^-	Equilibrium abundance
H_2^+	Equilibrium abundance
H_2	Rate equation
H_3^+	Equilibrium abundance
D^+	Rate equation
D	Conservation law
HD	Rate equation
He^+	Rate equation
He	Conservation law
C^+	Rate equation
C	Conservation law
C^-	Equilibrium abundance
O^+	Rate equation
O	Conservation law
O^-	Equilibrium abundance
Si^+	Rate equation
Si	Conservation law
Si^{++}	Rate equation
CH^+	Equilibrium abundance
CH_2^+	Equilibrium abundance
CH_3^+	Rate equation
CH	Rate equation
CH_2	Rate equation
OH^+	Equilibrium abundance
H_2O^+	Equilibrium abundance
H_3O^+	Equilibrium abundance
OH	Rate equation
H_2O	Rate equation

Table 1—Continued

Species	Method of solution
CO ⁺	Equilibrium abundance
CO	Rate equation
HOC ⁺	Equilibrium abundance
HCO ⁺	Rate equation
O ₂ ⁺	Equilibrium abundance
O ₂	Rate equation
C ₂	Rate equation
SiH ⁺	Equilibrium abundance

Table 2. Processes included in our thermal model.

Process	References
Cooling:	
Lyman- α cooling	Cen (1992)
He electronic excitation	Cen (1992); Bray et al. (2000)
Thermal bremsstrahlung	Shapiro & Kang (1987)
Compton cooling	Cen (1992)
H ₂ rotational, vibrational lines	Le Bourlot et al. (1999); Ripamonti & Abel (2004)
HD rotational, vibrational lines	Lipovka, Núñez-López, & Avila-Reese (2005)
Fine structure lines (C, C ⁺ , O, Si, Si ⁺)	Many sources; see papers I, III
CO rotational, vibrational lines	Neufeld & Kaufman (1993); Neufeld, Lepp & Melnick (1995)
H ₂ O rotational, vibrational lines	Neufeld & Kaufman (1993); Neufeld, Lepp & Melnick (1995)
OH rotational, vibrational lines lines	Pavlovski et al. (2002)
H ⁺ recombination	Ferland et al. (1992)
He ⁺ recombination	Aldrovandi & Pequignot (1973); Hummer & Storey (1998)
H & He collisional ionization	Janev et al. (1987)
H ₂ collisional dissociation	Many sources; see papers I, III
Heating:	
H ₂ gas-phase formation	Many sources; see papers I, III

Table 3. Physical state of the densest gas within the scale radius r_s at time t_{end}

Run	Z^{a} (Z_{\odot})	λ^{b}	$E_{\text{turb}}^{\text{c}}$ (E_{int})	$t_{\text{end}}^{\text{d}}$ (Myrs)	$T_{\text{c,min}}^{\text{e}}$ (K)	$n_{\text{c,max}}^{\text{f}}$ (cm^{-3})	$x_{\text{H}_2,\text{c,max}}^{\text{g}}$
Z0	0.0	0.0	0.0	53	79	$> n_{\text{sink}}$	2.9×10^{-3}
Z0-TURB1	0.0	0.0	0.05	71	66	$> n_{\text{sink}}$	3.2×10^{-3}
Z0-TURB2	0.0	0.0	0.1	50	82	3.5×10^2	2.8×10^{-3}
Z-3-TURB2	10^{-3}	0.0	0.1	65	66	1.6×10^4	3.0×10^{-3}
Z0-ROT	0.0	0.05	0.0	86	67	2.5×10^4	2.9×10^{-3}
Z-3-ROT	10^{-3}	0.05	0.0	70	59	1.5×10^4	2.9×10^{-3}
Z-1-ROT	10^{-1}	0.05	0.0	82	67	1.9×10^4	2.7×10^{-3}

^aMetallicity of the gas.

^bSpin parameter of the halo.

^cAdded turbulent energy in units of the initial internal energy.

^dTime at the end of the simulation.

^eMinimum temperature of the gas within the scale radius r_s .

^fMaximum number density of the gas within the scale radius r_s . $n_{\text{sink}} = 1.25 \times 10^5 \text{ cm}^{-3}$ is the threshold density for sink creation.

^gMaximum fractional H_2 abundance within the scale radius r_s .